Catalysis Today 422 (2023) 114213

Contents lists available at ScienceDirect

Catalysis Today

journal homepage: www.elsevier.com/locate/cattod

# Hybrid organometallo-silica catalysts for sustainable visible-light promoted olefin isomerization

Mónica Martínez-Aguirre [a], Elena Serrano [b], Cintia Ezquerro [a], Elena Lalinde [a], Jesús R. Berenguer [a,*], Javier García-Martínez [b,*], Miguel A. Rodríguez [a,*]

[a] Organometallic Molecular Materials (MATMO). Departamento de Química-Centro de Investigación en Síntesis Química (CISQ), Universidad de La Rioja Madre de Dios, 53, E-26006 Logroño, La Rioja, Spain
[b] Molecular Nanotechnology Lab. Departamento de Química Inorgánica. Universidad de Alicante. Ap. 99, E-03690 Alicante, Spain

ARTICLE INFO

*Keywords:*
Visible-light photocatalysis
Olefin isomerization
Organometallo-silica
Sol-gel coordination chemistry
Cyclometalated iridium(III) complex

ABSTRACT

The use of visible light as a clean and affordable reagent has turned photocatalysis into a green and powerful tool in synthetic chemistry. However, most of these photocatalytic processes are carried out under homogeneous conditions, which requires expensive catalysts that are difficult to recover and recycle. One way to overcome this problem is to incorporate the visible-active species into porous solid matrices. However, integrating these active species into the matrix to achieve a stable and active heterogeneous photocatalyst is not easy, and has usually been done by post-synthetic strategies. Herein, we describe the use of the highly emissive cyclometalated complex $[Ir(dfppy)_2(dasipy)]PF_6$ as a building block for the in-situ synthesis of four different silica-based heterogeneous photocatalysts, and a related post-synthetic grafted material. These highly stable materials have been assessed in the energy transfer photo-isomerization reaction of *trans*- to *cis*-stilbene under blue light and mild conditions; showing not only high isomerization yields (ca. 80 %), but also easy recovery and excellent recyclability (up to 100 % after 7 cycles).

## 1. Introduction

The use of visible light to drive chemical reactions has become one of the cleanest and more energy-efficient ways of addressing the tenants of sustainable and green chemistry [1–8]. Visible light-mediated photocatalysis can proceed through two main mechanisms: single electron transfer (SET) for photoredox reactions [4,9–11], and energy transfer (EnT) in photosensitized processes [7,12]. Both approaches involve fewer steps or require more friendly conditions than a thermal reaction [13–15]. To that end, a good number of aromatic organic chromophores and transition metal complexes, able to be excited under visible irradiation, have been used as photocatalysts [12,16].

The course of SET is strongly dependent on the relative oxidation and reduction potentials of excited photocatalysts and substrates, as the latter often have high redox potentials that prevent the reaction from succeeding. However, processes that occur through EnT depend mainly on the relative triplet state energies between substrates and photocatalysts and, therefore, photocatalysts must have a high-energy triplet state. Transition metal complexes are widely employed as either photoredox or EnT catalysts. This is mainly due to their high intersystem crossing efficiencies that usually lead to the quantitative population of triplet excited states, their tunable phophysical properties and outstanding photostability. A large number of studies refer to emissive octahedral $d^6$ Ir(III) and Ru(II) derivatives, because these species can undergo long-lived excited triplet states, metal-to-ligand charge transfers, and high photoluminescence quantum yields (ϕ) [17–20]. These complexes are typically used as homogeneous catalysts, which limits their industrial applications mainly due to: i) the need to purify the final products, and ii) the difficult recovery and recyclability of the expensive $d^6$ and $d^8$ catalysts [13,21]. To overcome these limitations several attempts have been made to design photocatalysts containing cheaper and more abundant transition metals such as copper, iron, molybdenum, or cerium [22–24]. Nevertheless, the properties of these catalysts still do not match those of the precious metals.

A promising strategy to overcome the afore-mentioned drawbacks is based on the integration of the homogeneous luminescent organometallic catalysts onto high surface area solid matrices. These systems present the well-known advantages of heterogeneous catalysis, such as

* Corresponding authors.
*E-mail addresses:* jesus.berenguer@unirioja.es (J.R. Berenguer), j.garcia@ua.es (J. García-Martínez), miguelangel.rodriguez@unirioja.es (M.A. Rodríguez).

https://doi.org/10.1016/j.cattod.2023.114213
Received 22 December 2022; Received in revised form 21 April 2023; Accepted 17 May 2023
Available online 19 May 2023
0920-5861/© 2023 The Author(s). Published by Elsevier B.V. This is an open access article under the CC BY-NC-ND license (http://creativecommons.org/licenses/by-nc-nd/4.0/).

easy recovery and reusability, while maintaining the high selectivity typical of homogeneous catalysts [25]. Several examples of this strategy include: (i) the encapsulation of metal complexes within zeolite cavities, MOFs, or ion-exchange resins; (ii) their grafting onto mesoporous inorganic oxides or plasmonic metal nanoparticles; and (iii) their intercalation within the interlayer space of layered materials such as graphene or nano $C_3N_4$ sheets [21,26–31]. Among these matrices, mesoporous silica is widely used as catalyst support due to their excellent properties, such as large surface area, tunable surface chemistry and porosity, and excellent stability (both chemical and thermal). Different morphologies, ranging from macroscopic nanostructured gels to monodisperse nanoparticles can be readily obtained by well-known sol-gel synthetic strategies [32–38]. In addition, silica is an abundant and cheap material that presents optical transparency in the visible region [39–41]. These features make it a suitable support for use as a photocatalyst, as has been shown in pioneering works by Professors Wu [42] and Yamashita [43,44]. In their research, Pt(II) or Ir(III) coordination complexes were employed. Similarly, Prof. Geraghty [45] demonstrated the use of organic compounds as visible-active species.

The incorporation of both coordination complexes [32,37,46–51] or organic compounds [34,52–54] to the mesoporous silica has usually been carried out by post-synthetic methods such as impregnation or grafting. These post-synthetic methods are used due to their versatility and high incorporation yields. However, and despite their widespread use, these techniques have several main drawbacks, namely (i) the possibility of aggregation of the active phase on the surface of the solid support, leading to (ii) partial blocking of the mesoporosity of silica supports, which decreases their accessible pore volume; and (iii) leaching of the active phase when used in fluid media, which limits its reuse. In addition, these methods involve several synthetic steps and longer preparation times. Therefore, there is a growing interest in the development of more straightforward strategies based on the in situ incorporation of the homogeneous photocatalysts during the gel-sol preparation of the silica. This approach leads to stable hybrid materials with a more homogeneous distribution of the photoactive species into the inorganic matrix, avoiding their agglomeration and/or leaching [25,38,55]. In line with this idea, in recent years our groups have delved the “Sol-Gel Coordination Chemistry” approach [38], which is based on the in situ co-condensation of organometallic complexes bearing alkoxysilane terminal groups with the adequate silica source. This *one*-pot method allows for the incorporation of a wide variety of functionalities (from nanoparticles to coordination complexes) into various mesoporous supports, allowing easy modulation of their textural, morphological and photophysical properties. This has led to the preparation of a series of organometallo-silica hybrid materials that have been successfully applied in catalysis, illumination, and bioimaging [56–59].

On the other hand, cyclometallated Ir(III) complexes, some of them with structures similar to those of the complexes we have previously incorporated on mesoporous silica supports, have been shown to be very efficient homogeneous photocatalysts in EnT visible-light photocatalyzed reactions [7,12]. Among the wide variety of EnT processes, the selective isomerization of alkenes to obtain the Z-isomer is a major challenge in organic synthesis. The difficulty of this process relies on the lower thermodynamic stability of the Z-conformation, which results in the formation of the more stable isomer E. However, Z conformation is often necessary for the preparation of anticancer drugs [60], chromatic lasers [61], or industrial dyes [62], among others. In addition, in the field of molecular switches, E-Z isomerization is of great relevance [63]. Traditional (i.e. non-photocatalytic) methods to obtain the Z isomer are often very expensive, energy-intensive [64–66], and usually lead to poor stereoselectivity. For this reason, the photoassisted E to Z isomerization reaction is usually carried out by irradiation under UV-light [60,67], but this approach is ineffective over a wide range of alkenes. Therefore, there is an active quest to find new ways to achieve this transformation under different conditions.

In this context, we have chosen the highly phosphorescent cyclometalated complex [Ir(dfppy)$_2$(*dasipy*)]$PF_6$ (**1**; dfppy = 2-(2,4)-difluorophenyl-pyridinyl; dasipy = N,N’-dipropiltriethoxysilane-2,2’-bipyridine-4,4’-dicarboxamide), because it emits at 550 nm (2.25 ev) [56], slightly above of the *trans*-stilbene’s triplet energy (580 nm, 2.14 ev) [68]. This complex is functionalized with two triethoxysilyl terminal groups that allow for their co-condensation with the silica source during the synthesis of the final materials. Hence, we draw on our experience on the synthesis of organometallo-silica materials to design five different mesoporous hybrid silica-based materials (including nanoparticles and amorphous silica gels), following both in situ and *post-synthetic* methods. The incorporation yields of the chromophore and the photophysical and textural properties of the five materials were studied. In a second step, the applicability of theses photocatalysts was evaluated in the isomerization reaction of the *trans*-stilbene [69,70].

The photo-isomerization reactions have been carried out under mild conditions, with blue light irradiation, and their kinetics and yields were easily trackable by $^1$H NMR. The photocatalytic results are discussed throughout the text in terms of quantum yield of the hybrid materials, chromophore accessibility, and chromophore stability. Despite their low chromophore loading (i.e. 0.2 – 1 wt%), all the as-synthesized hybrid organometallo-silica materials show high isomerization yields (ca. 80 %) along with enhanced reusability (up to 7 catalytic cycles for the in-situ materials).

## 2. Experimental section

Detailed Synthetic and General Methods are included in the Electronic Supplementary Information (ESI).

## 3. Results and discussion

### 3.1. Synthesis and characterization of the hybrid organometallo-silica catalysts

The highly emissive complex [Ir(dfppy)$_2$(*dasipy*)]$PF_6$ (**1**) was synthesized, as reported elsewhere [56], by reacting [Ir(dfppy)$_2$(NCMe)$_2$]$PF_6$ with the stoichiometric amount of the diamine ligand dasipy (see ESI, Scheme S1). This complex was used as starting building block for: i) the in situ *one-pot* synthesis of four different hybrid organometallo-silica materials, both gels (**$SiO_2$_N**, **$SiO_2$_B**, **$SiO_2$_OD**) and nanoparticles (**NP_IS**), and ii) the preparation of the related post-synthetic grafted silica nanoparticles **NP_G.**

Scheme 1 illustrates the synthesis (and nomenclature used) of the different hybrid organometallo-silica catalysts, which was adapted from our previously reported methodology for this kind of materials [56–58]. All of them were carried out under mild conditions – from room temperature (RT) to 80 °C (see Electronic Supplementary Information for details). The metallic content of each of the materials, as determined by Inductively Coupled Plasma (ICP) analysis, as well as their textural properties, are shown in Table 1.

The hybrid silica gels **$SiO_2$_N** and **$SiO_2$_B** were prepared in the absence of surfactant, using NaF as a catalyst for the co-condensation of tetraethyl orthosilicate (TEOS) with the alkoxysilane terminal groups of **1**, and in a neutral or basic media for **$SiO_2$_N** (i, Scheme 1) and **$SiO_2$_B** (ii, Scheme 1), respectively [58]. In both cases, a solution of the complex **1** and TEOS (in tetrahydrofuran, THF, for **$SiO_2$_N** or EtOH for **$SiO_2$_B**) was stirred in water at RT for 24 h, with the amount of complex **1** calculated to get a nominal iridium content of 1 wt%. Both approaches led to mesoporous materials, with surface areas in the range of 500–600 $m^2$/g, and high complex incorporation yields, ca. 70 % (see Table 1 and Fig. 1). Transmission Electron Microscopy (TEM) analysis confirms the amorphous and porous structure of these catalysts (see ESI, Fig. S1 and S2). Although not shown here for the sake of clarity, **$SiO_2$_B** showed very similar textural properties to the respective complex-free silica material previously synthesized under comparable basic

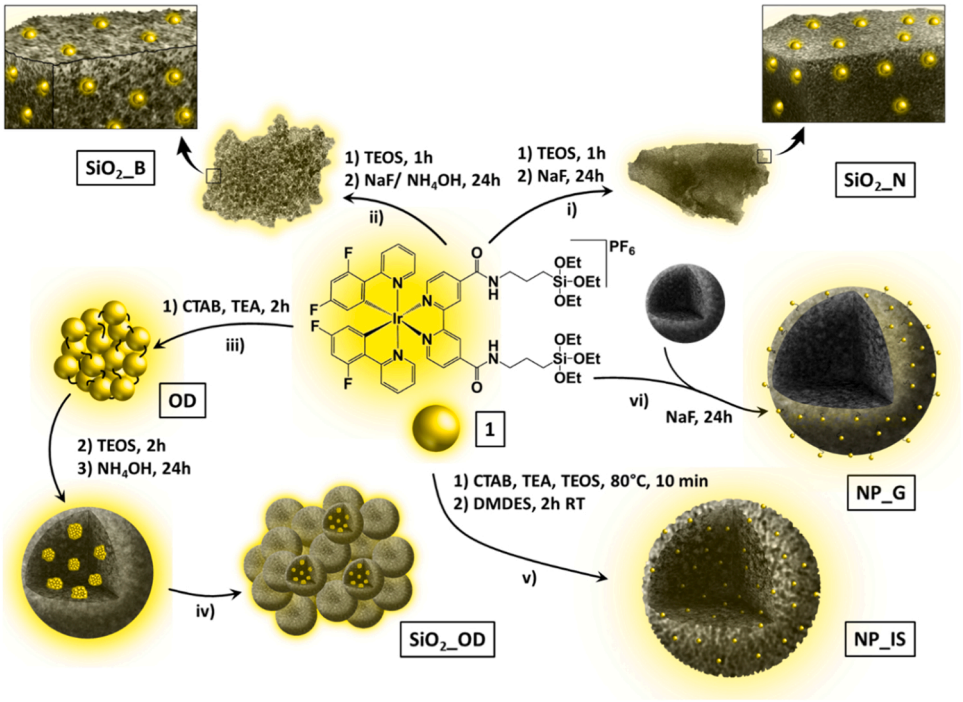


**Scheme 1.** Schematic representation of the syntheses of the hybrid organometallo-silica catalyst starting from complex [Ir(dfppy)$_2$(*dasipy*)]PF$_6$ (**1**), and nomenclature used.

**Table 1**
Metal content and textural properties of the mesoporous hybrid organometallo-silica materials.

| Sample | Ir[a] (wt%) | $A_{BET}$[b] ($m^2/g$) | $V_p^{0.99}$[c] ($cm^3/g$) | $d_p$[d] (nm) |
|---|---|---|---|---|
| $SiO_2$_B | 0.76 (1.0) | 465 | 0.8 | 9.7 |
| $SiO_2$_N | 0.71 (1.0) | 580 | 0.4 | 5.0 |
| $SiO_2$_OD | 0.38 (1.0) | 1270 | 2.0 | 4.0/13.0 |
| NP_IS[e] | 0.11 (0.2) | 1120 | 2.2 | 5.0 |
| NP_G | 0.89 (1.0) | 610 | 1.3 | 3.0 |

a) Iridium content calculated from ICP mass spectroscopy analyses after treatment of the samples with diluted HF. Values in brackets represent the nominal metal content.
b) Surface area estimated by the multipoint BET method using the adsorption data in the relative pressure ($P/P_0$) range of 0.05–0.3.
c) Total pore volume read directly from the adsorption branch of the isotherm at 0.99.
d) Average pore diameter determined at the maximum of the pore size distribution plot obtained applying the NLDFT equilibrium model.
e) Data obtained from reference [56]. Hybrid organometallo-silica gels, i.e. **$SiO_2$_N**, **$SiO_2$_B** and **$SiO_2$_OD**, were centrifuged and air dried before their textural characterization. All samples were degassed at 100 °C before gas adsorption measurements (see Experimental section for details).

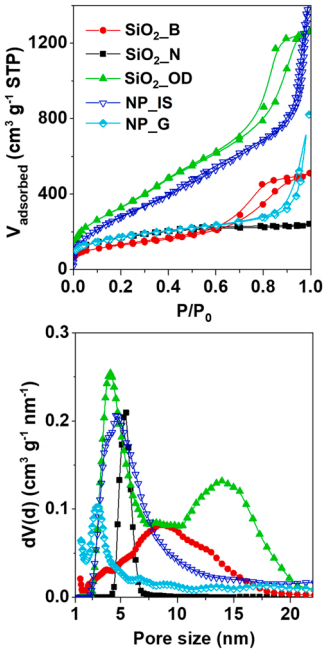


**Fig. 1.** $N_2$ adsorption/desorption isotherms at 77 K (up) and the corresponding pore size distribution calculated using the NLDFT method (bottom) of the mesoporous hybrid organometallo-silica materials.

conditions [58], with a total pore volume of ca. 0.8 $cm^3 \cdot g^{-1}$ and an average pore diameter of ca. 10 nm. In the case of **$SiO_2$_N**, the porosity was slightly blocked, which resulted in a reduced total pore volume and average pore diameter of the sample in comparison to the related silica-free material [58], as well as to the hybrids synthesized under basic media. This has been previously attributed to the lower interaction of cationic Ir(III) complexes with the silica precursor in a neutral medium [58].

**$SiO_2$_OD** and **NP_IS** were obtained using hexadecyltrimethylammonium bromide (CTAB) as a surfactant and triethanolamine (TEA) as the catalyst of the sol-gel processes. The synthesis of **$SiO_2$_OD** was also carried out to get a nominal iridium content of 1 wt%. This was done at RT in a one-pot two-steps procedure. In a first step, a solution of complex **1** in EtOH was pre-hydrolyzed in water for two hours in the presence of TEA and CTAB to achieve the growth of Organometallic Dots (**OD**, iii, Scheme 1) [57]. These particles, formed only by molecules of complex **1** covalently bonded through the condensation of the alkoxysilane terminal groups, were further reacted, in a second step, with TEOS in basic media for additional 24 h to obtain the final **$SiO_2$_OD** material (iv, Scheme 1). This catalyst is formed by aggregates of small mesoporous nanoparticles (see ESI, Fig. S3 and

below). For comparison purposes, we chose our recently reported **NP_IS** [56]. This material consists on discrete mesoporous organometallo-silica nanoparticles obtained by a 10 min reaction at 80 °C of an ethanolic solution containing both complex **1** and TEOS with a basic aqueous solution of CTAB and TEA. Subsequently, diethoxydimethylsilane (DMDES) was added and the mixture was stirred for 2 additional hours, leading to nanoparticles superficially capped with methyl groups (v, Scheme 1). The solid contained a nominal iridium content of 0.2 wt%. This material was selected because of its excellent textural and emissive properties, as discussed below [56]. Finally, in both cases (**$SiO_2$_OD** and **NP_IS**), CTAB was removed by ionic exchange with a saturated ethanolic solution of $NH_4NO_3$. Incorporation yields in the 40–60 % range were obtained for both materials by ICP analyses (Table 1). Besides their different morphologies, i.e. open amorphous and porous structure for **$SiO_2$_OD** and nearly monodispersed spherical shaped mesoporous particles of ca. 80 nm in the case of **NP_IS** (see ESI, Figs. S3 and S4), both hybrids have excellent textural properties, showing similar type IV isotherms with mesopore volumes of ca. 1.8 $cm^3 \cdot g^{-1}$, BET surface areas in the 1120–1270 $m^2 \cdot g^{-1}$ range, and a narrow pore size distribution of mesoporous, with an average size of ca. 4–5 nm (see Table 1 and Fig. 1). As expected, **$SiO_2$_OD** also shows large interparticle mesopores with a wider distribution between 10 and 20 nm.

Finally, a post-synthetic type of mesoporous silica nanoparticles with the complex **1** superficially grafted (**NP-G**) was obtained (Table 1 and Fig. 1, see also ESI Fig. S5). To that end, we prepared a complex-free conventional mesoporous silica nanoparticle (**MSN**, see Synthetic Methods in ESI), which were further suspended in EtOH and stirred at room temperature for 24 h with the appropriate amount of complex **1** (nominal iridium content of 1 wt%). The reaction was carried out in the presence of NaF to accelerate the hydrolysis of the alkoxy groups (Scheme 1). In addition to the high incorporation yield of iridium in **NP-G** (ca. 90 %), both the iridium-containing (**NP_G**) and metal-free NPs (**MSN**) show similar BET surface area (610 $m^2 \cdot g^{-1}$ vs. 760 $m^2 \cdot g^{-1}$, respectively) and total pore volume (1.3 $cm^3 \cdot g^{-1}$ vs. 1.2 $cm^3 \cdot g^{-1}$, respectively) [56].

The effective incorporation of complex **1** into the five materials and the preservation of their molecular structure were further analyzed by infrared, absorption, and emission spectroscopies (see Photophysical properties section for the latter). The FTIR spectra of all hybrid organometallo-silica materials, both gels and nanoparticles, show the bands corresponding to the Si–O and Si–O–Si bonds. In addition, all the spectra display weak characteristic absorptions of complex **1** at ca. 3280 $cm^{-1}$, 2900 $cm^{-1}$ and 1500–1400 $cm^{-1}$, which are due to the $\nu$(N–H) and the $\nu$(C–H) of the amidic groups, and the $\nu$(ring) of aromatic groups, respectively (see ESI, Synthetic methods and Fig. S6). Furthermore, two additional bands appear at ca. 1265 $cm^{-1}$ and 850 $cm^{-1}$ in the spectrum of the hybrid nanoparticles **NP_IS**, in agreement with the presence of the Si-Me bonds of the DMDES used as capping agent during their synthesis (see ESI, Synthetic methods for details).

### 3.2. Photophysical properties

Table S1 and S2 (see ESI) collect the absorption and emission data of complex **1** and all the hybrid organometallo-silica materials. Figs. 2 and S7-S9 (see ESI) show a selection of the corresponding spectra.

As reported elsewhere [56], the absorption spectra of complex **1** in both solid state (Diffuse Reflectance UV–vis, DRUV) and THF solution (see ESI, Fig. S7) show an intense absorption peak in the high energy region mainly due to spin-allowed intraligand π-π * transitions corresponding to both aromatic ligands dfppy (L: C^N) and dasipy (L': N^N) ($\lambda_{abs}$ < 300 nm), and to a mixture of intraligand and ligand-to-ligand [C^N →N^N] charge transfer transitions ($^1$IL/$^1$LL'CT) ($\lambda_{abs}$ 300–320 nm), with a certain contribution of the metal. A less intense absorption band is observed in the 340–400 nm range, owing to a mixture of metal–to–ligand [M→N^N] and ligand-to-ligand charge transfers ($^1$ML'CT/$^1$LL'CT). Finally, the spectra also show weak absorptions at lower energies ($\lambda_{abs}$ 400–500 nm) that are usually ascribed to spin-forbidden $^3$ML'CT/$^3$LL'CT transitions. As shown in Fig. 2a, the solid state DRUV spectra of all the organometallo-silica materials display similar absorptions to those described for complex **1**, including the lower energy features ($\lambda_{abs}$ > 400 nm), which proves that the structural integrity of the chromophore is preserved during the its incorporation to the silica matrix.

The emissive properties of complex **1** have also been recently described based on theoretical calculations [56]. In summary, complex **1** shows, in degassed THF solution, a bright yellow structureless phosphorescence (τ 0.71 μs, ϕ 56 %) with a maximum at 550 nm (Fig. S8 and Table S2 in ESI), which has been ascribed to a mixture of $^3$ML'CT/$^3$LL'CT transitions with a remarkable metallic contribution. In the solid state, the emission appears slightly red-shifted ($\lambda_{max}$ 560 nm) with reduced values of lifetime and PLQY (τ 0.35 μs, ϕ 29 %). This is consistent with the higher non-radiative constant observed in the solid state compared to THF solution, and is indicative of some degree of aggregation-caused-quenching (ACQ) in the solid-state associated to the occurrence of π···π interactions.

Excitation and emission spectra of the hybrid organometallo-silica materials were recorded in the solid state and in $CHCl_3$ suspension (1 mg/ML), as the latter is the medium in which the photocatalytic studies were carried out (vide infra). In both media, all the hybrid materials feature similar broad emission profiles to those observed for complex **1** in the solid state or THF solution (Fig. 2b; see also ESI, Fig. S9 and Table S2).

In detail, the hybrid silica gel **$SiO_2$_B** displays, in the solid state, the largest bathochromic shift with respect to complex **1** ($\lambda_{max}$ 580 nm vs. 560 nm). Nevertheless, the emission in chloroform suspension is clearly blue-shifted, appearing at the same wavelength to that observed for complex **1** in THF solution ($\lambda_{max}$ 550 nm). This clearly points to some degree of interaction of the solvent with the chromophore molecules, and, thus, the presence of a high proportion of complex molecules located on the surface of the material. On the other hand, the hybrid in

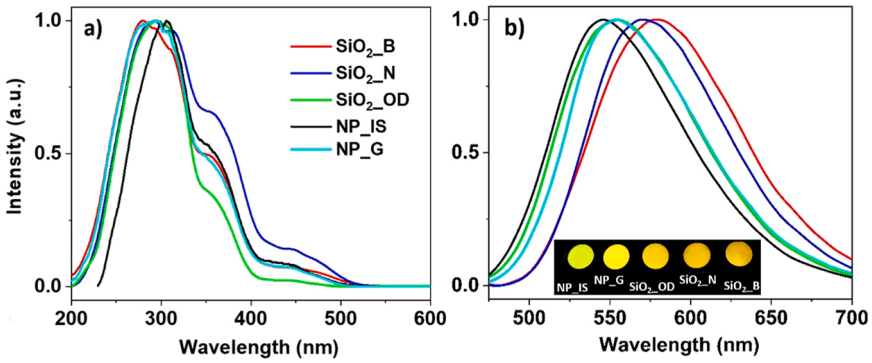


**Fig. 2.** Solid state DRUV (a) and emission spectra at room temperature ($\lambda_{exc}$ 365 nm, b) of the hybrid organometallo-silica materials.

situ materials **$SiO_2$_N** and **$SiO_2$_OD** show in the solid state the emission maxima at 570 and 555 nm, respectively, but in $CHCl_3$ suspension both emissions appear at the same maxima ($\lambda_{max}$ 565 nm). These three materials, **$SiO_2$_B, $SiO_2$_N** and **$SiO_2$_OD**, show the lowest PLQY, both in solid state and suspension ($\phi$ 10.0 – 15.8 %). Considering the ACQ characteristics of complex **1** in the solid state, this observation might be expected for **$SiO_2$_OD**, for which the initial formation of the Organometallic Dots (**ODs**) implies the condensation of very close chromophore molecules, and this clearly indicates a high degree of association of the chromophore molecules in the silica gels **$SiO_2$_B** and **$SiO_2$_N**.

The energy emission maximum of the discrete nanoparticles **NP_IS**, with a $\lambda_{max}$ 550 nm, does not depend on the measurement medium (solid state or suspension), which is consistent with a very good shielding of the chromophores, and coincides with that of complex **1** in THF solution at room temperature ($\lambda_{max}$ 550 nm). Furthermore, this is by far the most emissive in situ material, with PLQY (ϕ 50.1 % in solid state, and 42.6 % in suspension) similar to that observed for the chromophore **1** in THF (ϕ 55.8 %). Thus, **NP_IS**, which is the material with the lowest iridium content (0.11 wt%), is the solid in which the molecules of the complex are better dispersed and protected by the silica matrix, which prevents solid aggregation quenching and better mimics the behavior of the chromophore in solution.

Finally, the grafted nanoparticles **NP_G** show the emission maximum at 555 nm in the solid state, which is slightly blue-shifted in suspension ($\lambda_{max}$ 550 nm). In contrast to our previous observations for related nanoparticles containing only 0.2 wt% of Ir, which showed a high PLQY of ca. 39 % [56], **NP_G** features in the solid state a PLQY of only 16 %. This is likely due to the higher incorporation of the iridium chromophore in **NP_G** (4.5-fold in mass, 0.89 wt% Ir), which surely facilitates some degree of quenching by aggregation of the iridium molecules on the silica surface. Indeed, its PLQY dramatically increases in $CHCl_3$ suspension (ϕ 46 %), thus suggesting that the interaction of the solvent with the grafted Iridium(III) complexes reduces both the intermolecular π···π quenching between the chromophore molecules and the non-radiative constant.

All the hybrids feature longer lifetime in $CHCl_3$ suspension than in solid state (see ESI, Table S2). This increase is particularly remarkable for **NP_G** and **$SiO_2$_B**, whose lifetime are more than double (τ 0.97 μs vs. 0.42 μs for **NP_G**, and 0.89 μs vs. 0.29 μs for **$SiO_2$_B**). In addition, the low energy absorptions (DRUV spectra, Fig. 2a) and the excitation maxima at $\lambda_{abs} > 400$ nm observed for all the hybrids, both in solid state and suspension (see ESI, Fig. S9), make them suitable candidates for the study of photocatalytic processes under blue illumination.

### 3.3. Photocatalytic studies

Encouraged by these results, the photocatalytic performance of the hybrids in the *trans*- to *cis*-stilbene isomerization reaction was assessed (Fig. 3), and the results were compared to those of cyclometalated complex **1** used as homogeneous photocatalyst (Fig. S10, see also Table 2). This reaction is a well-known process, which evolution is easily quantifiable by $^1$H NMR spectra (see ESI for details). As such, NMR tubes were used as reactors. Inside them, different photocatalysts:*trans*-stilbene mixtures were irradiated with blue LED light, using a RGB LED of 50 W, at RT (see ESI for details).

First, the photoreaction induced by **1** at both 1:0.05 and 1:0.02 *trans*-stilbene:complex **1** molar ratios was studied. Although the reaction is slightly slower using a molar ratio of 1:0.02 than a molar ratio of 1:0.05 ($k'_{0.05}/k'_{0.02} = 1.54$, Table 2), after 1.5 h of irradiation both reach 85 % *cis*-stilbene conversion (see ESI, Fig. S10). The same experiment was run under non-irradiating conditions (i.e. in absence of blue LED light) and no conversion to the *cis*-isomer was observed after 6 h of reaction, which evidences the photocatalytic nature of this process.

The same procedure was then carried out using each of the five silica-based materials as photosensitizer (see ESI for details). As shown in Table 2 and Fig. 3b, all materials were photoactive, reaching a maximum

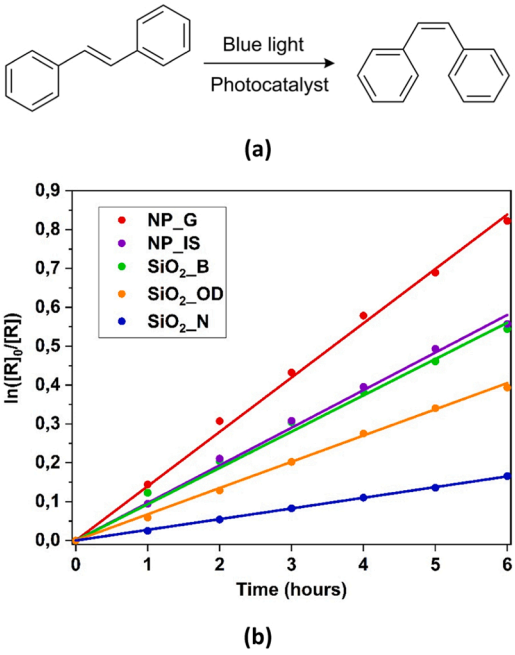


**Fig. 3.** (a) Photocatalytic *trans*- to *cis*-stilbene isomerization reaction. (b) Representation of the pseudophotocatalytic constant (k') of the five hybrid materials for the first 6 h of the reaction.

**Table 2**
Constant values of the photocatalytic activity, regression coefficients, and conversions reached at different times for each photocatalyst.

| Photocatalyst | Conversion at 6 h (%) | Maximum conversion (%) / Time (h) | k' ($h^{-1}$)[a)] | R[b)] |
|---|---|---|---|---|
| Complex 1[c)] | 85 | 85 / 1.0 | 1.337 ± 0.021 | 0.9995 |
| Complex 1[d)] | 85 | 85 / 1.5 | 2.066 ± 0.006 | 0.9999 |
| $SiO_2$_B[d)] | 50 | 82 / 25 | 0.093 ± 0.002 | 0.9989 |
| $SiO_2$_N[d)] | 20 | 73 / 53 | 0.028 ± 0.001 | 0.9999 |
| $SiO_2$_OD[d)] | 33 | 80 / 27 | 0.068 ± 0.001 | 0.9998 |
| NP_IS[c)] | 47 | 79 / 23 | 0.097 ± 0.002 | 0.9992 |
| NP_G[d)] | 59 | 83 / 16 | 0.140 ± 0.002 | 0.9994 |

a) 1st order reaction rate pseudophotocatalytic constant of the reaction of isomerization of *trans*-stilbene into *cis*-stilbene obtained as the average of three runs.
b) Regression coefficient.
c) *trans*-stilbene:photocatalyst molar ratio = 1:0.02.
d) *trans*-stilbene:photocatalyst molar ratio = 1:0.05.

conversion of ca. 80 % after an exposure time ranging from 16 to 53 h, in the following order of reactivity: **NP_G** (16 h, 83 %) > **NP_IS** (23 h, 79 %) ≥ **$SiO_2$_B** (25 h, 82 %) > **$SiO_2$_OD** (27 h, 80 %) > **$SiO_2$_N** (53 h, 73 %). The explanation for this trend is far from straightforward, and might be mainly attributed to a synergistic contribution of two different factors, the quantum yield ($\phi$) of the catalysts and the accessibility to the metal centers, which depends on surface area, pore volume, and pore diameter, among others. Thus, the material with the best photocatalytic performance (**NP_G,** Table 2) is the one that presents at the same time the highest quantum yield in $CHCl_3$ suspension (ϕ 46 %, See ESI Table S2) and the best accessibility to the chromophore molecules, which are covalently grafted onto the surface of the silica nanoparticles. Despite being very different materials, **NP_IS** and **$SiO_2$_B** are the next

most reactive ones, displaying quite similar activity ($k'_{NP\text{-}G}/k'_{NP\text{-}IS}$ or $_{SiO2\_B} \approx 1.5$, Table 2). **$SiO_2$_B** is a disordered gel showing low quantum yield in suspension ($\phi \sim 16$ %) and discrete textural properties (e.g., $A_{BET}$ 580 $m^2g^{-1}$, Table 1). Nevertheless, accordingly to its photophysical properties, it is thought to maintain a high fraction of complex molecules onto the material surface, which can facilitate the interaction with the substrate. By contrast, **NP_IS** consists of discrete nanoparticles with the chromophore in smaller and better protected quantity (nominal iridium content of 0.2 wt% vs. 1 wt% for the rest of hybrid catalysts) within the silica matrix. These characteristics that should lead to poorer catalytic results, however, seem to be compensated by a high surface area and mesopore volume ($A_{BET}$ 1120 $m^2g^{-1}$, $V_p$ 2.2 $cm^3g^{-1}$) and excellent quantum yield in suspension ($\phi$ 42.6 %). **$SiO_2$_OD** exhibits twice less photoactivity than **NP_G** ($k'_{NP\text{-}G}/k'_{SiO2\_OD} = 2.1$, Table 2), which might be ascribed to a discrete quantum yield of 10.4 % in $CHCl_3$ suspension, in spite of having the best textural properties ($A_{BET}$ 1270 $m^2g^{-1}$, $V_p$ 2.0 $cm^3g^{-1}$). Not unexpectedly, the least reactive catalyst is **$SiO_2$_N** ($k'_{NP\text{-}G}/k'_{SiO2\_N} = 5$, Table 2), which features the worst combination of textural ($A_{BET}$ 465 $m^2g^{-1}$, $V_p$ 0.8 $cm^3g^{-1}$) and emissive ($\phi$ 12.5 %) properties.

Next, the recyclability of the hybrids was evaluated by performing a total of seven photocatalytic cycles of six hours each. After each catalytic cycle, the hybrids were recovered by centrifugation, washed with dichloromethane and then re-used in successive cycles (see ESI for details). The results obtained reveal that, even after seven cycles, all materials showed high photostability (Fig. 4), pointing to their good recoverability and reusability for this kind of photoreactions. In fact, the efficiency loss results for all materials (See ESI, Fig. S11) are well-correlated with their corresponding textural and photophysical properties. Thus, the materials with the least protected chromophore (**NP_G** and **$SiO_2$_B**) presented the highest decrease in their photocatalytic activity (ca. 20 %), maybe due to the partial lixiviation of the Ir(III) molecules during the reaction or the cleaning procedure of the catalysts. In contrast, the hybrids containing the chromophores in a more protected environment, i.e. **$SiO_2$_OD** or **NP_IS**, showed a smaller decrease (**$SiO_2$_OD**, ca. 10 %) or even no variation (**NP_IS**) in their photoactivity throughout the seven recycling cycles. Surprisingly, although **$SiO_2$_N** is the least photoactive catalyst, its activity increases steadily with the recycling cycles (28 %), which seems to indicate a better exposure of the Ir(III) molecules to the medium with time. Also, no signals corresponding to free complex **1** were detected by $^1$H NMR in any of the reaction media for any of the hybrid materials. Finally, we have also selected the two samples showing the best catalytic performances, i.e. **NP_IS** and **NP_G**, to test their photophysical properties after completing the recyclability studies. Both samples are also archetypal examples of materials prepared by in situ and post-synthetic methods, respectively. As shown in the ESI (Table S3 and Fig. S12), after seven catalytic cycles of six hours each, both materials maintain similar emission profiles with a small decrease of their quantum yield (20 % for **NP_IS** vs. 30 % for **NP_G**) and a slight bathochromic shift of the emission maximum for **NP_G**.

## 4. Conclusions

Three texturally different silica gels (**$SiO_2$_N**, **$SiO_2$_B**, **$SiO_2$_OD**) and discrete nanoparticles (**NP_IS**) were produced by the co-condensation of the highly emissive cyclometalated complex [Ir(dfppy)$_2$(*dasipy*)]$PF_6$ (**1**) and tetraethyl orthosilicate (TEOS). Using a conventional *post-synthetic* method, we also synthetized related grafted silica nanoparticles (**NP_G**). In spite of their different textural properties, all the materials show well-developed mesoporosity, surface areas ranging from 465 to 1270 $m^2g^{-1}$, and high Ir(III) complex incorporation yields (40–90 %). All the materials display similar absorption and emission profiles confirming the preservation of the complex (**1**) structure during the incorporation method. Nevertheless, in $CHCl_3$ suspensions, while the three silica gels (**$SiO_2$_N**, **$SiO_2$_B**, **$SiO_2$_OD** $\phi \approx 13$ %) show an emissive behavior similar to that observed for complex **1** in the solid state, both nanoparticles (**NP_IS**, **NP_G**. $\phi \approx 44$ %) essentially mimic the behavior of complex **1** in solution.

Considering that all the materials display weak energy absorptions and excitation maxima at $\lambda_{exc} > 400$ nm, we studied their activity and recyclability as heterogeneous photocatalysts in the isomerization of

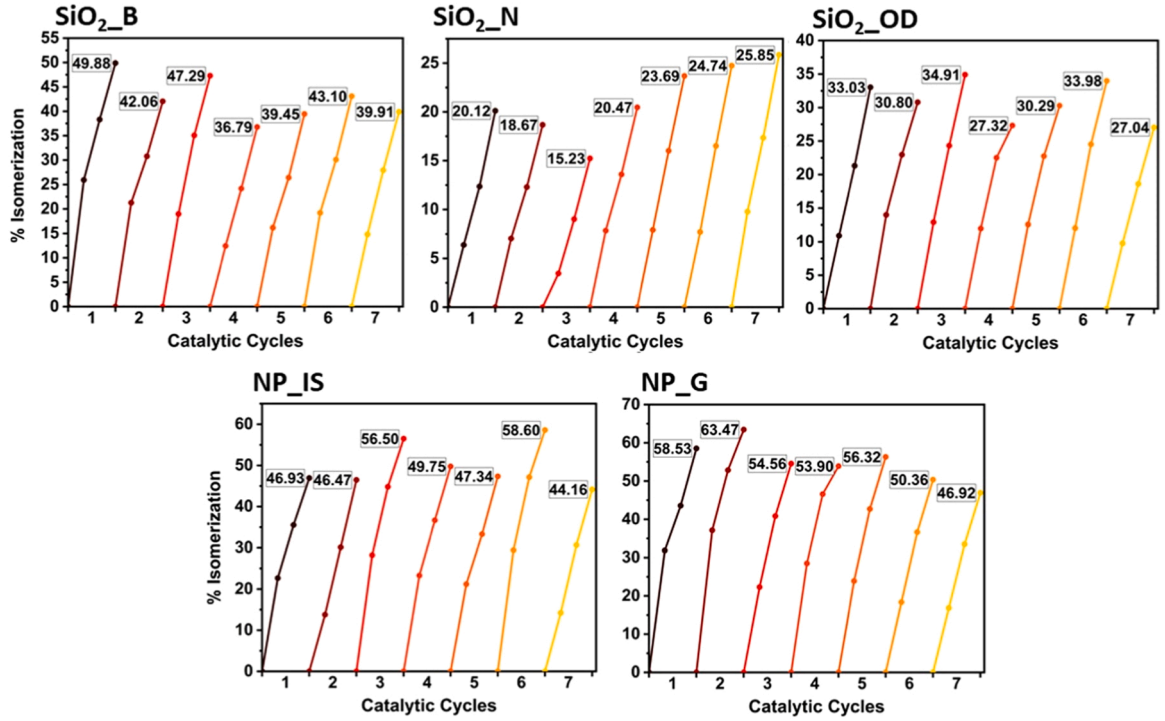


**Fig. 4.** Isomerization results obtained after 6 h of reaction for the hybrid materials during each of the seven catalytic cycles. Experiments were carried out under identical conditions.

*trans*- to *cis*-stilbene in $CDCl_3$, under blue illumination and mild conditions. Although our materials show less catalytic activity than complex **1** (homogeneous), all the hybrid catalysts present comparable conversion yields (~80 %), negligible Ir(III) leaching, easy recovery, and excellent stability and recyclability. The differences in the catalytic activities of each of the materials should be attributed to a synergistic combination of chromophore accessibility and their emissive properties, suggesting that an increase in the lifetime and/or quantum yield of the material improves the photocatalytic efficiency of the material. Accordingly, **NP_G** is the most active catalyst, showing the highest quantum yield in suspension; however, it is also is the material with the greatest loss of activity over successive catalytic cycles (ca. 20 %), which is probably related to the location of all the chromophore molecules at the silica surface in this material.

**NP_IS** is the material with the second-highest photocatalytic activity. The sample **NP_IS**, despite being the hybrid material with the lowest amount of chromophore, it shows the best combination of quantum yield and surface area, and, unlike **NP_G**, it retains almost 100 % of its catalytic activity after seven recycles. These results point out the versatility and many opportunities of the rational use of in situ synthetic approaches for the design of superior hybrid photocatalysts.

To sum up, we have realized the potential of hybrid organometallosilicas as very stable heterogeneous photocatalyst for EnT processes under visible illumination, paving the road to efficient heterogenisation of other relevant homogeneous photocatalytic reactions. On this context, a number of both energy transfer processes based on the generation of oxygen active species and single electron transfer photocatalyzed reactions are currently being studied in our laboratory.

## CRediT authorship contribution statement

**Mónica Martínez-Aguirre:** Formal analysis, Investigation, Methodology, Validation. **Elena Serrano:** Data curation, Funding acquisition, Methodology, Software, Writing - original draft. **Cintia Ezquerro:** Formal analysis, Methodology, Validation. **Elena Lalinde:** Formal analysis, Validation, Writing - original draft. **Jesús R. Berenguer:** Funding acquisition, Project administration, Writing - review & editing. **Javier García-Martínez:** Funding acquisition, Project administration, Writing - review & editing. **Miguel A. Rodríguez:** Conceptualization, Funding acquisition, Supervision, Writing - review & editing.

## Declaration of Competing Interest

The authors declare that they have no known competing financial interests or personal relationships that could have appeared to influence the work reported in this paper.

## Data availability

Data will be made available on request.

## Acknowledgements

This work was supported by the Spanish MCIN/AIE/10.13039/501100011033, the ''ERDF A way of making Europe'', the ''European Union'' (projects PID2019-109742GB-I00 and PID2021-128761OB-C21), Gobierno de la Rioja (Project FORTALECE 2021/01) and Generalitat Valenciana (Regional Project AICO/2021/037 - Conselleria d'Innovació, Universitats, Ciència i Societat Digital).

## Appendix A. Supporting information

Supplementary data associated with this article can be found in the online version at doi:10.1016/j.cattod.2023.114213.

## References

[1] P. Melchiorre, Chem. Rev. 122 (2022) 1483–1484.
[2] W. Yao, E.A. Bazan-Bergamino, M.-Y. Ngai, ChemCatChem 14 (2022), e202101292.
[3] T. Rigotti, J. Alemán, Chem. Commun. 56 (2020) 11169–11190.
[4] A. Jain, C. Ameta, Kinet. Catal. 61 (2020) 242–268.
[5] H. Lai, J. Zhang, F. Xing, P. Xiao, Chem. Soc. Rev. 49 (2020) 1867–1886.
[6] G. Masson, B. König, Eur. J. Org. Chem. 2020 (2020) 1191–1192.
[7] Q.-Q. Zhou, Y.-Q. Zou, L.-Q. Lu, W.-J. Xiao, Angew. Chem. Int. Ed. 58 (2019) 1586–1604.
[8] C. Stephenson, T. Yoon, D.W.C. MacMillan, Visible Light Photocatalysis in Organic Chemistry, Wiley-VCH, Weinheim, Germany, 2018.
[9] M. De Abreu, P. Belmont, E. Brachet, Eur. J. Org. Chem. 2020 (2020) 1327–1378.
[10] N. Corrigan, S. Shanmugam, J. Xu, C. Boyer, Chem. Soc. Rev. 45 (2016) 6165–6212.
[11] C.K. Prier, D.A. Rankic, D.W.C. MacMillan, Chem. Rev. 113 (2013) 5322–5363.
[12] F. Strieth-Kalthoff, M.J. James, M. Teders, L. Pitzer, F. Glorius, Chem. Soc. Rev. 47 (2018) 7190–7202.
[13] C. Kerzig, O.S. Wenger, Chem. Sci. 10 (2019) 11023–11029.
[14] L. Marzo, S.K. Pagire, O. Reiser, B. König, Angew. Chem. Int. Ed. 57 (2018) 10034–10072.
[15] J.J. Douglas, M.J. Sevrin, C.R.J. Stephenson, Org. Process Res. Dev. 20 (2016) 1134–1147.
[16] K.L. Skubi, T.R. Blum, T.P. Yoon, Chem. Rev. 116 (2016) 10035–10074.
[17] W.-P. To, Q. Wan, G.S.M. Tong, C.-M. Che, Trends Chem. 2 (2020) 796–812.
[18] X. Zhang, Y. Hou, X. Xiao, X. Chen, M. Hu, X. Geng, Z. Wang, J. Zhao, Coord. Chem. Rev, 417, 2020, 213371.
[19] F. Glaser, C. Kerzig, O.S. Wenger, Angew. Chem. Int. Ed. 59 (2020) 10266–10284.
[20] K. Teegardin, J.I. Day, J. Chan, J. Weaver, Org. Process Res. Dev. 20 (2016) 1156–1163.
[21] K. Mori, H. Yamashita, Chem. Eur. J. 22 (2016) 11122–11137.
[22] W.-M. Cheng, R. Shang, ACS Catal. 10 (2020) 9170–9196.
[23] L. Traub, O. Reiser, Phys. Sci. Rev. 4 (2019) 20170172.
[24] T.P. Nicholls, A.C. Bissember, Tetrahedron Lett. 60 (2019), 150883.
[25] S.L. Suib, J. Přech, J. Čejka, Y. Kuwahara, K. Mori, H. Yamashita, Mater. Today 32 (2020) 244–259.
[26] A. Eskandari, M. Jafarpour, A. Rezaeifard, M. Salimi, Appl. Organomet. Chem. 33 (2019), e5093.
[27] A. Kunzmann, S. Valero, Á.E. Sepúlveda, M. Rico-Santacruz, E. Lalinde, J. R. Berenguer, J. García-Martínez, D.M. Guldi, E. Serrano, R.D. Costa, Adv. Energy Mater. 8 (2018), 1702583.
[28] Y.-X. Tan, S.-X. Lin, C. Liu, Y. Huang, M. Zhou, Q. Kang, D. Yuan, M. Hong, Appl. Catal. B 227 (2018) 425–432.
[29] M. Wen, K. Mori, Y. Kuwahara, T. An, H. Yamashita, Chem. Asian J. 13 (2018) 1767–1779.
[30] K. Mori, D. Tatsumi, T. Iwamoto, Y. Masui, M. Onaka, H. Yamashita, Chem. Asian J. 13 (2018) 1348–1356.
[31] Y. Zhao, Y. Dong, F. Lu, C. Ju, L. Liu, J. Zhang, B. Zhang, Y. Feng, J. Mater. Chem. A 5 (2017) 15380–15389.
[32] P. Verma, Y. Kuwahara, K. Mori, R. Raja, H. Yamashita, Nanoscale 12 (2020) 11333–11363.
[33] X. Li, S. Ye, Y.C. Zhang, H.P. Zhao, Y. Huang, B. Zhang, T. Cai, Nanoscale 12 (2020) 7595–7603.
[34] S.M. Soria-Castro, B. Lebeau, M. Cormier, S. Neunlist, T.J. Daou, J.-P. Goddard, Eur. J. Org. Chem. 2020 (2020) 1572–1578.
[35] G. Mohammadi Ziarani, S. Rohani, A. Ziarati, A. Badiei, RSC Adv. 8 (2018) 41048–41100.
[36] M.P. Conley, C. Copéret, C. Thieuleux, ACS Catal. 4 (2014) 1458–1469.
[37] M. Rimoldi, A. Mezzetti, Catal. Sci. Technol. 4 (2014) 2724–2740.
[38] E. Serrano, N. Linares, J. Garcia-Martinez, J.R. Berenguer, ChemCatChem 5 (2013) 844–860.
[39] L. Li, W. Wang, J. Tang, Y. Wang, J. Liu, L. Huang, Y. Wang, F. Guo, J. Wang, W. Shen, L.A. Belfiore, Nanoscale Res. Lett. 14 (2019) 190.
[40] C.C. de Escobar, A. Dallegrave, M.A. Lasarin, J.H. Zimnoch dos Santos, Colloids Surf. A 486 (2015) 96–105.
[41] X. Qian, K. Fuku, Y. Kuwahara, T. Kamegawa, K. Mori, H. Yamashita, ChemSusChem 7 (2014) 1528–1536.
[42] K. Feng, R.-Y. Zhang, L.-Z. Wu, B. Tu, M.-L. Peng, L.-P. Zhang, D. Zhao, C.-H. Tung, J. Am. Chem. Soc. 128 (2006) 14685–14690.
[43] K. Mori, K. Watanabe, M. Kawashima, M. Che, H. Yamashita, J. Phys. Chem. C 115 (2011) 1044–1050.
[44] K. Mori, M. Tottori, K. Watanabe, M. Che, H. Yamashita, J. Phys. Chem. C 115 (2011) 21358–21362.
[45] R.A. Doohan, N.W.A. Geraghty, Green Chem. 7 (2005) 91–96.
[46] Y. Liang, Nanoscale Adv. 3 (2021) 6827–6868.
[47] M. Abd El Sater, N. Jaber, E. Schulz, ChemCatChem 11 (2019) 3662–3687.
[48] D. González-Muñoz, A. Casado-Sánchez, I. del Hierro, S. Gómez-Ruiz, S. Cabrera, J. Alemán, J. Catal. 373 (2019) 374–383.
[49] A.E. Fernandes, A.M. Jonas, Catal. Today 334 (2019) 173–186.
[50] H. Heinz, C. Pramanik, O. Heinz, Y. Ding, R.K. Mishra, D. Marchon, R.J. Flatt, I. Estrela-Lopis, J. Llop, S. Moya, R.F. Ziolo, Surf. Sci. Rep. 72 (2017) 1–58.
[51] A. Jana, J. Mondal, P. Borah, S. Mondal, A. Bhaumik, Y. Zhao, Chem. Commun. 51 (2015) 10746–10749.
[52] N. Body, C. Lefebvre, P. Eloy, T. Haynes, S. Hermans, O. Riant, J. Photochem. Photobiol. A 440 (2023), 114648.

[53] S.E. Mora-Rodríguez, A. Camacho-Ramírez, J. Cervantes-González, M.A. Vázquez, J.A. Cervantes-Jauregui, A. Feliciano, A. Guerra-Contreras, S. Lagunas-Rivera, Org. Chem. Front. 9 (2022) 2856–2888.
[54] D. González-Muñoz, A. Gómez-Avilés, C.B. Molina, J. Bedia, C. Belver, J. Alemán, S. Cabrera, J. Mater. Sci. Technol. 103 (2022) 134–143.
[55] N. Linares, E. Serrano, M. Rico, A. Balu, E. Losada, R. Luque, J. García-Martínez, Chem. Commun. 47 (2011) 9024–9035.
[56] C. Ezquerro, I. López, E. Serrano, E. Alfaro-Arnedo, E. Lalinde Peña, I. Larráyoz, J. G. Pichel, J. García-Martinez, J.R. Berenguer, Mater. Adv. 3 (2022) 3582–3592.
[57] C. Ezquerro, E. Fresta, E. Serrano, E. Lalinde, J. García-Martínez, J.R. Berenguer, R. D. Costa, Mater. Horiz. 6 (2019) 130–136.
[58] C. Ezquerro, A.E. Sepulveda, A. Grau-Atienza, E. Serrano, E. Lalinde, J. R. Berenguer, J. Garcia-Martinez, J. Mater. Chem. C 5 (2017) 9721–9732.
[59] N. Linares, A.E. Sepulveda, J.R. Berenguer, E. Lalinde, J. Garcia-Martinez, Microporous Mesoporous Mater. 158 (2012) 300–308.
[60] A.E. McCalley, S. Kaja, A.J. Payne, P. Koulen, Molecules 19 (2014) 7327–7340.
[61] M. Hara, S. Samori, X. Cai, M. Fujitsuka, T. Majima, J. Phys. Chem. A 109 (2005) 9831–9835.
[62] D.H. Song, H.Y. Yoo, J.P. Kim, Dyes Pigments (2007) 727–731.
[63] D. Cameron, S. Eisler, J. Phys. Org. Chem. 31 (2018), e3858.
[64] A.W.H. Speed, T.J. Mann, R.V. O'Brien, R.R. Schrock, A.H. Hoveyda, J. Am. Chem. Soc. 136 (2014) 16136–16139.
[65] Z. Huang, E.-i Negishi, J. Am. Chem. Soc. 129 (2007) 14788–14792.
[66] B. Tomassy, A. Zwierzak, Synth. Commun. 28 (1998) 1201–1214.
[67] N. Hoffmann, Chem. Rev. 108 (2008) 1052–1103.
[68] J. Saltiel, G.-E. Khalil, K. Schanze, Chem. Phys. Lett. 70 (1980) 233–235.
[69] H. Li, H. Chen, Y. Zhou, J. Huang, J. Yi, H. Zhao, W. Wang, L. Jing, Chem. Asian J. 15 (2020) 555–559.
[70] K. Singh, S.J. Staig, J.D. Weaver, J. Am. Chem. Soc. 136 (2014) 5275–5278.